

Geochemistry, Geophysics, Geosystems

RESEARCH ARTICLE

10.1029/2019GC008433

Key Points:

- More than 750 new SKS splitting measurements are made near Mount St. Helens, Washington
- Splitting parameters exhibit a 90° periodicity with back azimuth resulting from systematic error in standard measurement methods
- Corrected results indicate a substantial anisotropic layer with a fast axis parallel to subduction

Supporting Information:

- Supporting Information S1
- Table S1
- Table S2
- Table S3

Correspondence to:

C. M. Eakin,
caroline.eakin@anu.edu.au

Citation:

Eakin, C. M., Wirth, E. A., Wallace, A., Ulberg, C. W., Creager, K. C., & Abers, G. A. (2019). SKS splitting beneath Mount St. Helens: Constraints on subslab mantle entrainment.

Geochemistry, Geophysics, Geosystems,
20, 4202–4217. <https://doi.org/10.1029/2019GC008433>

Received 3 MAY 2019

Accepted 29 JUL 2019

Accepted article online 5 AUG 2019

Published online 27 AUG 2019

SKS Splitting Beneath Mount St. Helens: Constraints on Subslab Mantle Entrainment

C. M. Eakin¹ , E. A. Wirth² , A. Wallace³, C. W. Ulberg⁴ , K. C. Creager⁴ , and G. A. Abers⁵ 

¹Research School of Earth Sciences, The Australian National University, Canberra, ACT, Australia, ²U.S. Geological Survey, University of Washington, Seattle, WA, USA, ³ConocoPhillips School of Geology and Geophysics, University of Oklahoma, Norman, OK, USA, ⁴Department of Earth and Space Sciences, University of Washington, Seattle, WA, USA, ⁵Department of Earth and Atmospheric Sciences, Cornell University, Ithaca, NY, USA

Abstract Observations of seismic anisotropy can provide direct constraints on the character of mantle flow in subduction zones, critical for our broader understanding of subduction dynamics. Here we present over 750 new SKS splitting measurements in the vicinity of Mount St. Helens in the Cascadia subduction zone using a combination of stations from the iMUSH broadband array and Cascades Volcano Observatory network. This provides the highest density of splitting measurements yet available in Cascadia, acting as a focused “telescope” for seismic anisotropy in the subduction zone. We retrieve spatially consistent splitting parameters (mean fast direction Φ : 74°, mean delay time δt : 1.0 s) with the azimuthal occurrence of nulls in agreement with the fast direction of splitting. When averaged across the array, a 90° periodicity in splitting parameters as a function of back azimuth is revealed, which has not been recovered previously with single-station observations. The periodicity is characterized by a sawtooth pattern in Φ with a clearly defined 45° trend. We present new equations that reproduce this behavior based upon known systematic errors when calculating shear wave splitting from data with realistic seismic noise. The corrected results suggest a single layer of anisotropy with an ENE-WSW fast axis parallel to the motion of the subducting Juan de Fuca plate; in agreement with predictions for entrained subslab mantle flow. The splitting pattern is consistent with that seen throughout Cascadia, suggesting that entrainment of the underlying asthenosphere with the subducting slab is coherent and widespread.

1. Introduction

The Cascadia subduction zone, where the Juan de Fuca plate subducts beneath western North America, is one of the most intriguing subduction zones in the world (Figure 1a). An ominous seismic quiescence, yet known potential for a great $M9$ earthquake (Atwater et al., 2005; Goldfinger et al., 2012), has led to our reliance on geophysical instrumentation and numerical modeling techniques to better understand the dynamics and unique character of this subduction zone (e.g., Frankel et al., 2018; Wirth et al., 2018). In addition, it has recently been suggested that the subslab mantle buoyancy and flow field are important controls on the degree of plate locking and associated seismic hazard in Cascadia (Bodmer et al., 2018). Beneath the Pacific Northwest there has been a long history of subduction since about 150 Ma (Severinghaus & Atwater, 1990), with various fragmented remnants of the ancient Farallon plate imaged in the deep mantle beneath North America (Pavlis et al., 2012). At present, a very young (<10 Ma), and thus relatively thin (<50 km), Juan de Fuca plate is subducting and undergoing significant slab rollback with trench retreat rates of 3.6 cm/year (Hayes et al., 2018; Müller et al., 2008; Schellart et al., 2008).

Another intriguing feature of the Cascadia subduction zone is the puzzling nature of the surrounding mantle flow field, particularly the extent of toroidal versus entrained mantle flow in response to slab rollback (for a recent review on the topic of the “Cascadia Paradox,” see Long, 2016). In subduction dynamics, mantle flow is considered to follow an entrained flow pattern when it is coupled with and moving in the same direction as the downgoing slab. Conversely, toroidal flow generally refers to mantle flow that escapes from the subslab to the mantle wedge in a circular pattern around the slab edge. In this scenario there is a component of subslab mantle flow that is trench parallel, as opposed to purely trench normal in the entrained case. (We refer the reader to Figure 3 of Long (2016) if further explanation is required). One of the most direct methods by which to map the mantle flow patterns is by studying seismic anisotropy (i.e., the directional dependence of

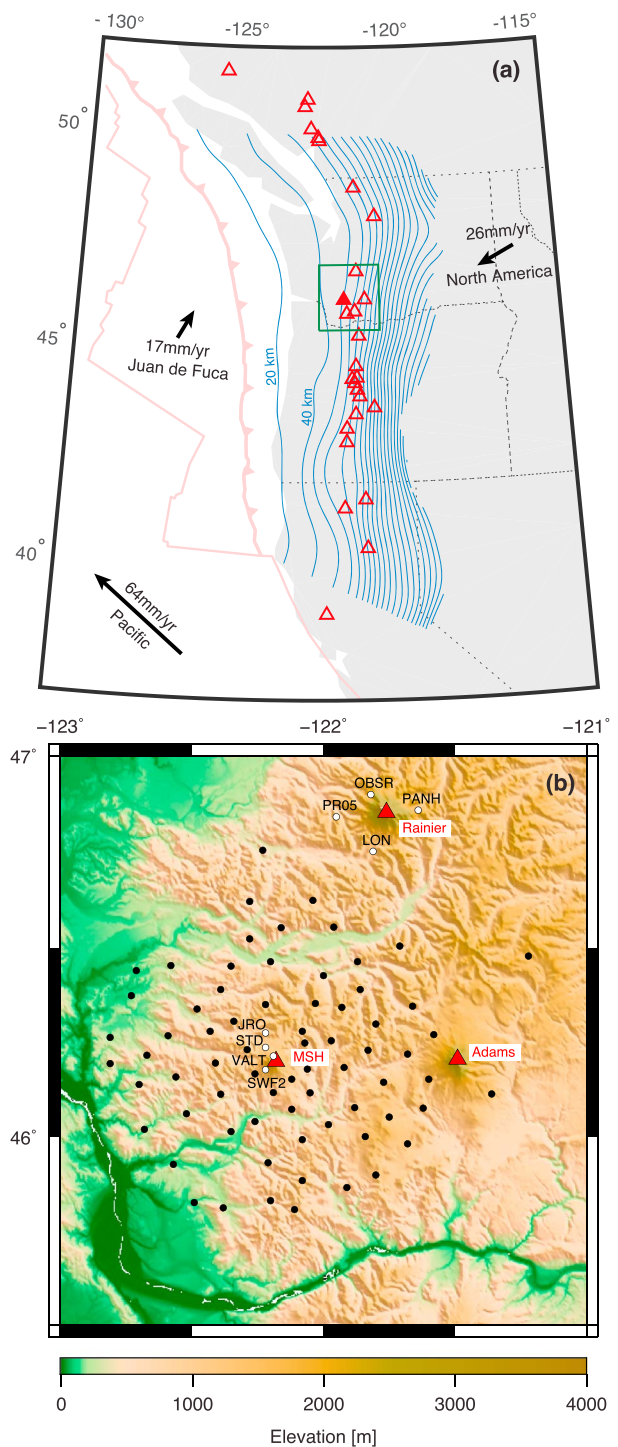


Figure 1. Regional tectonic setting of the Pacific Northwest showing location of the iMUSH broadband seismic array. (a) Outline of the Cascadia subduction zone where the Juan de Fuca plate subducts beneath North America as delineated by the blue contours (20-km increments) based on the Slab2 model (Hayes et al., 2018). Absolute plate motion vectors in black are from HS3-NUVEL1A (Gripp & Gordon, 2002). Volcanoes in the Cascade arc are shown by red triangles, with Mount St. Helens in solid red (Siebert & Simkin, 2002). (b) Map of the 78 broadband seismic stations used in this study. The regional location is given by the green box in (a). The distribution of 70 iMUSH (Imaging Magma under St. Helens) temporary stations are shown by the black dots. Station names can be found in Figure S1 in the supporting information. Solid white circles with attached names (black text) highlight eight permanent stations belonging to the Cascades Volcano Observatory (CVO). The three major active volcanoes in the area, Mount Rainier, Mount Adams, and Mount St. Helens (MSH) are shown by the solid red triangles.

seismic wave speed). Under typical upper mantle conditions (A-, C-, or E-type olivine fabrics), the fast axes of the constituent olivine crystals are thought to develop a lattice-preferred orientation (LPO) aligned with the mantle flow direction (Karato et al., 2008; Zhang & Karato, 1995). However, the dominant olivine fabric type will depend on the temperature, stress and hydration conditions in each individual subduction zone, and thus the exact relationship between deformation geometry and the fast axis orientation can be ambiguous. The study of seismic anisotropy can therefore provide insight into not only the dynamics of subduction in the deep Earth but also the physical and chemical conditions of the mantle.

Beneath the Cascadia forearc and trench, as well as offshore beneath the incoming Juan de Fuca plate, seismically observed fast axes are consistently found to align with the plate motion direction of the subducting Juan de Fuca slab (Bodmer et al., 2015; Currie et al., 2004; Eakin et al., 2010; Martin-Short et al., 2015; Rieger & Park, 2010). While this is in general agreement with entrained mantle flow, such a scenario is surprising given the complexity of seismic anisotropy patterns inferred in other subduction zones worldwide. In addition, one might expect the significant rollback of the Juan de Fuca slab to promote trench-parallel subslab mantle flow (Long & Silver, 2008). Widespread entrainment is also somewhat contradictory with the large-scale toroidal mantle flow that has been proposed for Cascadia (Zandt & Humphreys, 2008) to explain patterns of volcanism and anisotropy in the Cascadia backarc (Long et al., 2009, 2012).

The iMUSH (Imaging Magma under St. Helens; <https://imush.pnsn.org/>) seismic array, centered upon Mount St. Helens (MSH) in Washington State (Figure 1b), offers a unique opportunity to study seismic anisotropy and mantle flow directly beneath the Cascades volcanic arc where competing hypotheses for entrained (forearc) versus toroidal (backarc) mantle flow collide. The station spacing of this array (~10 km) is much denser than that of the EarthScope Transportable Array (~70 km; <http://usarray.org>), allowing for iMUSH stations to collectively act as a focused telescope into the Cascadia subduction zone beneath MSH (Creager et al., 2017; Ulberg et al., 2017). By combining seismic observations across the 70 stations that make up the array, a level of detail can be achieved that is not possible with a single station, particularly in terms of the azimuthal coverage of events. This allows for the careful analysis of possible back azimuthal patterns present in the splitting parameters, typically associated with the ability to identify more complex anisotropic structures such as multiple and/or dipping layers of anisotropy. This has been deemed critical to resolving the Cascadia Paradox (Long, 2016) but until now was not easily achievable with previous temporary arrays with larger station spacing (e.g., Eakin et al., 2010).

Here we present a new dense data set of SKS splitting measurements from the iMUSH broadband array and nearby permanent seismic networks. We retrieve consistent shear wave splitting parameters that match the broader pattern seen across the Cascadia subduction zone. Analysis of the back azimuth dependence of our results verifies the presence of a substantial mantle layer entrained beneath the subducting Juan de Fuca plate as has been previously suggested (Currie et al., 2004; Eakin et al., 2010; Long & Silver, 2009; Martin-Short et al., 2015). Additional thinner and shallower layers of anisotropy (e.g., in the wedge and overriding crust) are also compatible with our results but are unconstrained by the present SKS data set. Integration of these results with future iMUSH studies, such as local S splitting, will help to complete our picture of the anisotropic structure and upper mantle dynamics beneath MSH.

2. Shear Wave Splitting: Methodology and Data

We compute shear wave splitting measurements of distant teleseismic SKS phases. When a shear wave, such as an SKS phase, enters an anisotropic medium it becomes polarized into two quasi shear waves, a fast and a slow direction, in a process akin to optical birefringence. In shear wave splitting analyses, we typically measure the orientation of the fast direction (Φ) and magnitude of the delay time (δt) between the fast and slow arrivals. The delay time is proportional to both the strength and spatial extent of anisotropy. Outer core refracted phases, such as SKS, are particularly useful as they isolate the anisotropic signature of the mantle beneath the receiver (i.e., directly beneath the seismic station). Any anisotropy that may be present on the downward leg, between the seismic source and core, is removed when the S wave converts to a P wave at the core-mantle boundary.

For SKS phases, the primary source region of seismic anisotropy that generates the observed splitting is thought to lie in the upper mantle due to the lattice preferred orientation of olivine (Nicolas & Christensen, 1987). When the upper mantle undergoes deformation (i.e., flow) in the dislocation creep

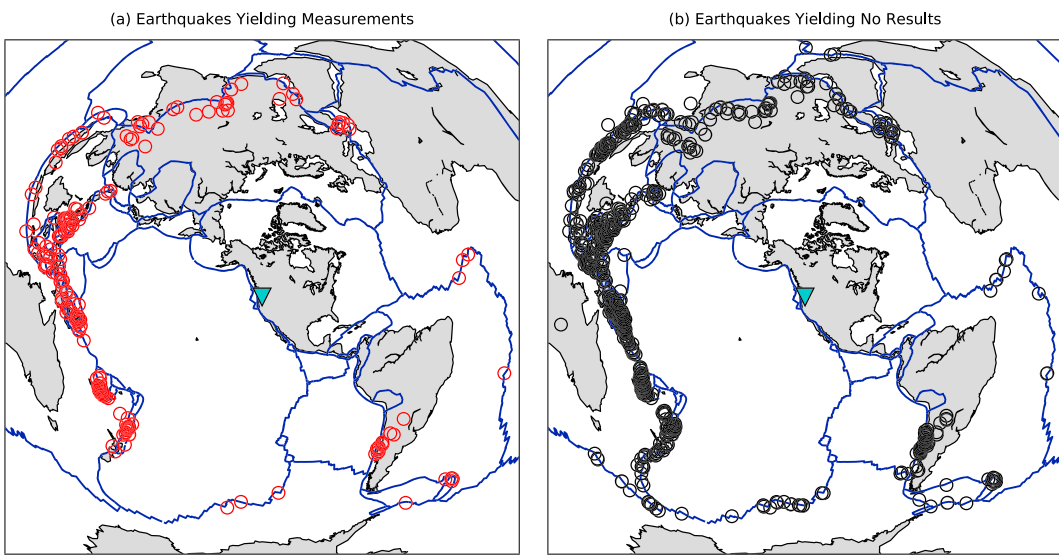


Figure 2. Distribution of the 937 events used in this study. Those that yielded a split or null result are indicated on the left by red open circles (a), and on the right those that did not return any result in black (b). The location of Mount St. Helens and the iMUSH array is represented by the inverted cyan triangle. iMUSH = Imaging Magma under St. Helens.

regime, anisotropic minerals such as olivine undergo a rotation relative to the strain geometry (e.g., Karato et al., 2008). The nonrandom distribution of crystallographic axes results in an effective bulk anisotropy that is ultimately detectable by seismic waves. Other potential source regions of anisotropy include the lowermost mantle in the D'' layer (Kendall & Silver, 1996), fossilized frozen-in anisotropy in the lithosphere (Silver & Chan, 1991), and crustal anisotropy due to the shape-preferred orientation (SPO) of fluid-filled cracks (e.g., Crampin, 1994). These various anisotropic contributions are usually minor in comparison to asthenospheric LPO due to their relatively limited spatial extent (Long & Becker, 2010). In a subduction zone like Cascadia, anisotropic hydrous phases, such as serpentine, may also contribute to the anisotropic signature (Mainprice & Ildefonse, 2009; McCormack et al., 2013).

This study uses data from a combination of temporary and permanent seismic networks in the vicinity of MSH (Figure 1). The iMUSH broadband array was comprised of 70 broadband seismic stations that operated from 2014–2016 (network code: XD; https://doi.org/10.7914/SN/XD_2014). Station spacing on average was less than 10 km (Figure 1b). In addition, we included data from eight long-running permanent seismic stations in the region. Four of these were situated near MSH (JRO, STD, SWF2, and VALT), the other four near Mount Rainier (LON, OBSR, PANH, and PR05). All of these stations belong to the Cascades Volcano Observatory (CVO; network code: CC; <https://doi.org/10.7914/SN/CC>) with the exception of station LON, which is operated by the Pacific Northwest Seismic Network at the University of Washington (network code: UW; <https://doi.org/10.7914/SN/UW>). The longest running of these stations is LON, from which we utilized data since 2002.

We analyze all teleseismic events in the epicentral distance range 90–130° of magnitude 6.0 and above for the presence of SKS splitting. At this distance SKS arrivals have almost vertical incidence (i.e., <10°). We identified 131 such events that occurred during the timespan of the iMUSH array, and 923 events that were recorded by one of our permanent stations. The distribution of events is more plentiful in the western quadrants but a wide range of azimuths is available (Figure 2). In total, 8,631 waveforms were available for shear wave splitting analysis.

Shear wave splitting analyses were performed using the SplitLab software package of Wüstefeld et al. (2008). Within this application, predictions of shear wave splitting parameters (fast direction Φ , delay time δt) are compared from two independent measurement methods: the transverse component minimum energy (SC) method of Silver and Chan (1991), and rotation correlation (RC) method (Bowman & Ando, 1987). SplitLab also calculates splitting parameters for the eigenvalue (EV) method, but this is broadly equivalent to the SC method for SKS phases (Silver & Chan, 1991). We therefore focused our attention on comparison of

the independent RC and SC measurement methods, and only retained measurements that yielded consistent estimates between both. An example is provided in the supporting information (Figure S2). Henceforth, we choose to discuss the results from the RC method, unless otherwise stated, as it is independent of the initial polarization (i.e., the back azimuth for SKS phases). Any misalignment in the station orientation, or deviation of the incoming SKS polarization, will impact the quality and accuracy of splitting measurements made via the SC method (Eakin et al., 2018; Liu & Gao, 2013), leading to greater variability. It is worth noting that the RC method is known to produce a systematic 45° deviation at near-null back azimuths (Wüstefeld & Bokelmann, 2007). This is a well-defined and predictable outcome, which we will utilize in section 4.

A band-pass filter was applied to all waveforms with corner frequencies of 0.02 and 0.125 Hz to reduce noise. For permanent stations, the lower corner frequency was raised to 0.04 Hz. This is in accordance with the optimal filter determined through spectral analysis and filtering tests of Restivo and Helffrich (1999), along with previous SKS studies in Cascadia (e.g., M. D. Long et al., 2009) and other subduction zones (Eakin et al., 2015; Eakin & Long, 2013; Wirth & Long, 2010). In Figures S3–S5 it is shown that increasing the upper corner to include higher frequencies (up to 0.2 Hz) does not change the general character of our splitting data set, but it does result in noisier seismograms and degrades the signal-to-noise ratio (SNR; Figure S5). Increased noise on the transverse component increases the likelihood that spuriously correlated noise may be mistaken for shear wave splitting, while at the same time increases the minimum delay time threshold at which SKS splitting can be observed, as smaller delay times with smaller amplitudes on the transverse component will be obscured. We find that a band-pass filter with an upper corner frequency of 0.125 Hz produces the best SNR for SKS phases and the most well constrained results (Figure S3).

Following our previous work (Eakin et al., 2015; Wirth & Long, 2010), all splitting measurements were visually inspected and subject to strict quality control, with both quantitative and qualitative conditions applied. Quantitative conditions included a SNR cutoff greater than 5, and errors less than 1 s in ∂t and less than 22.5° in Φ at the 95% confidence level. Additionally, we required agreement between the RC and SC methods to be within $|\Phi| < 22.5^\circ$, and $\partial t_{RC}/\partial t_{SC} > 0.7$ following (Wüstefeld & Bokelmann, 2007). Qualitative measures included the observation of similarly shaped shear wave pulses on the estimated fast and slow directions, minimal energy on the corrected transverse component, and linearization of the particle motion following the correction for splitting. An example of a well-constrained splitting measurement is shown in Figure S2a.

Observations of null SKS arrivals were also recorded in this study. For a null measurement, we require a clearly visible shear wave pulse on the radial component with little energy on the uncorrected transverse component (i.e., linear uncorrected particle motion). Again, we applied a SNR cutoff greater than 5. For an example of a null measurement, see Figure S2b. In general, null arrivals suggest that the SKS phase has not undergone any splitting. When coupled with non-null measurements, a null measurement can indicate that the incoming SKS polarization (i.e., the back azimuth) is aligned with either a fast or slow axis of anisotropy.

3. SKS Splitting Results

Overall our SKS splitting analysis yielded 757 measurements across all 78 stations (Figures 3–6). A full list is provided in Table S1 in the supporting information. The majority of the measurements were recorded as null (77%; 584 out of 757). The remaining 173 non-null (i.e., split) measurements returned consistent ENE-WSW splitting (mean Φ : 74° , mean ∂t : 1.04 s) across the entire array, and similar to those measured by previous studies in the region (Figure 3). However, as seen in Figure 3b, most iMUSH stations generated only a single split. Only 89 split measurements were retrieved for 70 iMUSH stations compared to 410 nulls, representing an average of one split and six nulls per station. For the eight CVO stations the percentage of splits was higher with an average of 11 splits and 29 nulls per station (84 splits and 174 nulls in total). However, over the same 2014–2016 recording period with the same availability of events, CVO stations record two splits and six nulls per station, very similar to the numbers retrieved at iMUSH stations.

Despite the large number of nulls retrieved by this study, they appear consistent with an ENE-WSW fast direction of anisotropy (Figures 4 and 5). The majority of null measurements are found on events with back azimuths in the range 60 – 90° . This agrees exceptionally well with the fast directions found from the more limited splitting measurements (blue bars in Figure 4). In addition, splits and nulls tend to be recorded at

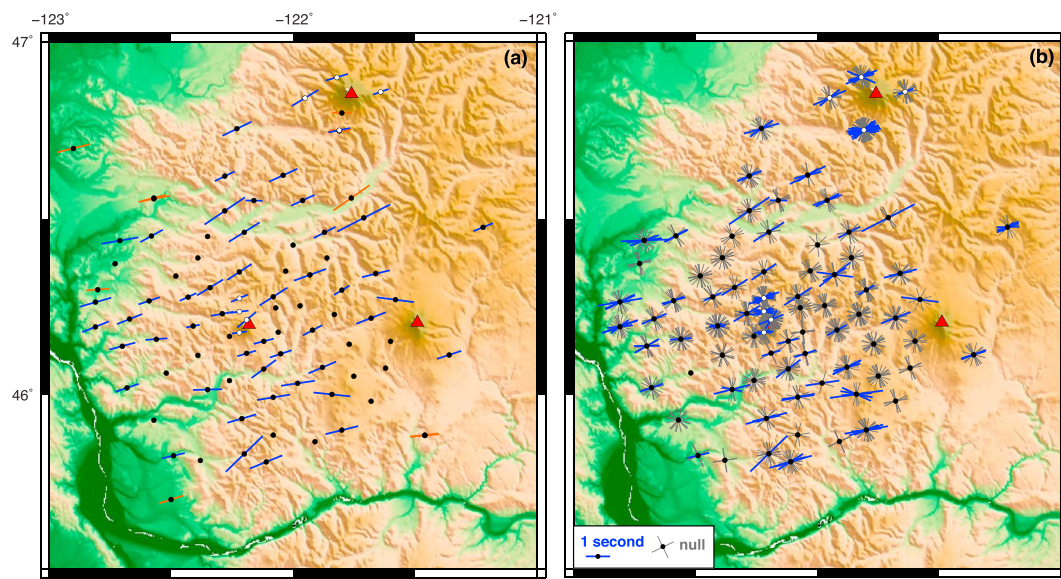


Figure 3. Map of average (a) and individual (b) shear wave splitting measurements retrieved at each station. Non-null measurements (i.e., splits) are represented by blue bars aligned with the fast direction (ϕ) and scaled by the delay time (δt) according to the legend shown. Null measurements are indicated by gray crosses aligned with the back azimuth indicating a potential fast and slow orientation. Previous measurements in the vicinity made by earlier studies are shown in orange [Bodmer et al., 2015; Currie et al., 2004; Eakin et al., 2010; Long et al., 2009; Martin-Short et al., 2015; Silver & Chan, 1991; Vinnik et al., 1992].

different back azimuths, yet their distribution and relative abundance do not appear to be controlled by the availability of events (Figure 5). All together this indicates that the nulls are most likely to be generated when

the event back azimuth, and therefore the initial polarization of the SKS wave, is already aligned with a fast (~75°) or slow (~165°) orientation. We note that some nulls, albeit fewer in number, are still present across all back azimuths (Figures 4 and 5). This is likely due to noise on the seismogram which can obscure the splitting signal on the transverse component, particularly if it is weak, resulting in a null observation (Liu & Gao, 2013). Overall, it is insightful that the back azimuths at which splits and nulls are most (or least) likely to occur are anticorrelated (Figure 5), suggesting that their distribution is reflective of the anisotropy. Detailed recording of nulls, as we have performed here, can therefore be valuable and informative in helping to characterize the underlying anisotropic structure.

Across the iMUSH array there appears to be little lateral variability in splitting parameters (Figures 3 and S6), suggestive of a common anisotropic structure at depth. In the asthenosphere, the Fresnel zone of SKS waves (i.e., the region over which the waves are sensitive to anisotropy) has a width of 136 km at 200-km depth (Gudmundsson, 1996). Given our small 10-km station spacing, the width of the iMUSH array (Figure 1b) extending from 123°W to 121.5°W is only ~165 km, which is comparable to the width of the SKS Fresnel zones in the upper mantle. Therefore, for most iMUSH stations, SKS phases with near vertical incidence (<10°) will overlap considerably throughout the upper mantle with sensitivity to the same underlying mantle volume; thus, this explains why the splitting parameters are so similar from station to station. This uniquely dense array acts as a focused telescope into the mantle beneath MSH, allowing us to combine all our results to analyze subtler

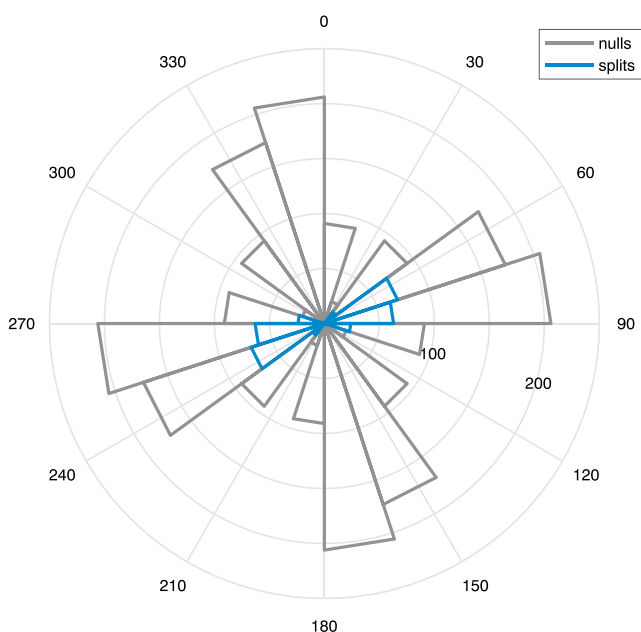


Figure 4. Rose diagram of the fast direction (ϕ) found by results across all stations. Similar to Figure 3, both the back azimuth and orthogonal to the back azimuth are plotted for nulls (in gray), as either is a potential fast orientation. The majority of split (blue) and null (gray) results are in agreement for an ENE-WSW fast direction.

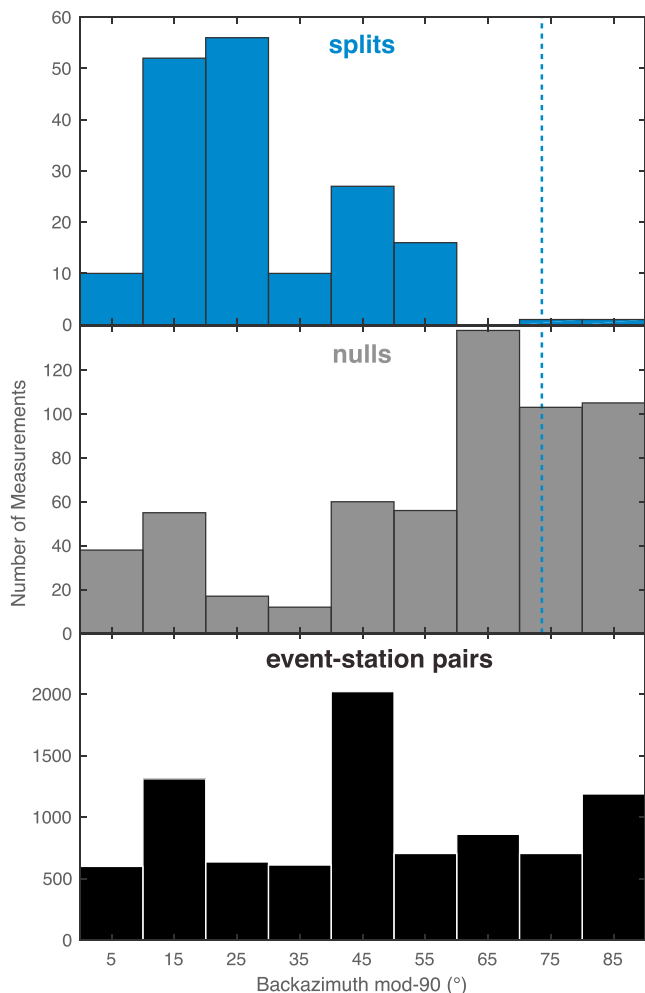


Figure 5. Histogram of the number and type of measurements made according to back azimuth (modulated over 90°). (top panel) Dashed blue line is the average fast direction of the splits (mean $\Phi = 74^\circ$). The bottom panel (black bars) indicates the total number and back azimuthal distribution of event-station pairs available to this study.

The characteristic differences between the RC and SC methods described by Wüstefeld and Bokelmann (2007) were primarily based on synthetic seismograms with SNRs of 15 and moderate delay times (1.3 s). As seen in Figure S5 a SNR of 15 is unusually high for real data with SNRs of 5–10 more typical for measurable events. If instead the results of the same set of synthetic tests are compared for seismograms with a more realistic SNR of 5 and input delay time of 1.0 s (similar to the characteristics of our data set) then both the RC and SC methods generate a 45° trend in Φ (Figure 7) similar to what we observe (Figures 6a–6d). It is notable that the fast direction is much more scattered for SC, but that the greatest deviation still occurs at back azimuths close to the fast axis orientation where a sharp change or discontinuity in Φ also occurs. This is likely a consequence of the SC method becoming less reliable and predictable at near null back azimuths, where it generates a wide range of possible values (Wüstefeld & Bokelmann, 2007). Those that by chance happened to agree with the results of the RC method would have been classified as splits, based on our measurement criteria. The 45° trend in Φ retrieved by the SC method in our results is therefore likely due to the requirement that the two methods should be in agreement (Figures 6 and 7). The results of the SC method will therefore have a tendency to mimic the RC method, especially when the SNR is relatively low, and the SC method is more scattered over a greater back azimuthal range.

This apparent misbehavior of our measurement methods in the presence of realistically noisy seismograms is actually helpful in that the RC method produces systematic errors that are well constrained and

variations and make more robust interpretations that are not possible using just a single station.

4. Interpreting Variation in Splitting Parameters With Back Azimuth

When all the results are combined and the splitting parameters (Φ and δt) are plotted as a function of back azimuth, interesting patterns emerge (Figures 6a–6d). In particular, the observed fast directions increase (i.e., rotate clockwise) from 0–60° back azimuths, followed by a sharp change at back azimuths of 60–75° (Figures 6a and 6c). The location of this sharp change is consistent with the back azimuthal distribution of nulls in Figure 5 which also peak at 60–70°. This 90° periodicity with back azimuth is a clear yet intriguing feature of our data set. Importantly, the rotation of the observed fast direction follows a sawtooth pattern with a well-defined 45° slope ($\Phi = \text{back azimuth } \pm 45^\circ$). This pattern is seen for both the RC and SC methods but is most pronounced for the RC method. It cannot be reproduced by multiple layers of anisotropy (Figure S8), which only produce a 45° trend approaching the null lines (dotted black lines) in Figures 6a and 6c ($\Phi = \text{back azimuth } \pm 90^\circ$).

Similar patterns with 45° trends have been observed previously in synthetic tests by Monteiller and Chevrot (2010), Vecsey et al. (2008); and Wüstefeld and Bokelmann (2007), as well as briefly noted by Menke and Levin (2003). In Wüstefeld and Bokelmann (2007), characteristic differences between the RC and SC methods were used to define a null classification system whereby it was observed that the measured fast direction tends to differ by 45° between the two methods when the back azimuth approaches the fast/slow axis orientation. At such back azimuths, the RC delay time tends to zero. This is easily explained within the context of the rotation correlation method. For null observations where all the SKS energy is contained on the radial (Q) component, and none on the transverse (T) component, a maximum in cross correlation between the two horizontal components is found when Q and T are rotated 45°. In such cases the SKS energy on Q will be subdivided equally between the test fast and slow components producing identical waveforms on each component with a zero time lag.

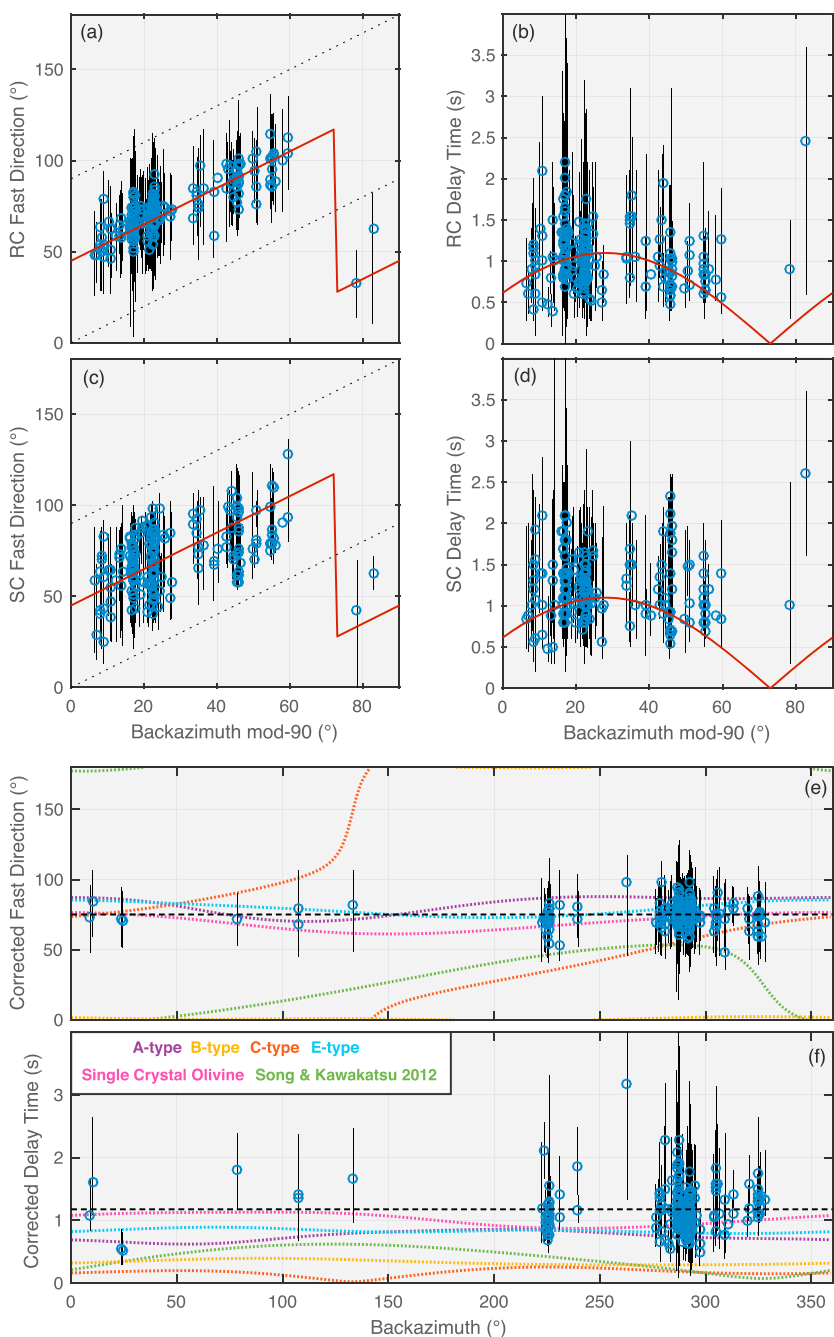


Figure 6. Splitting parameters (Φ and ∂t) with respect to back azimuth. SKS splitting results (blue circles with black error bars) display clear trends and 90° periodicity for both the RC method (a, b) and SC method (c, d). The results follow the predictions of systematic error (red line, equations (1) and (2)) by Wüstefeld and Bokelmann (2007), which would be expected for a single anisotropic layer with a fast direction of 73° and delay time of 1.1 s (Figures 7 and S7). The dotted black line in (a) and (c) indicates values where splitting would not occur, where the fast direction equals the back azimuth $\pm 90^\circ$. In Figures 6e and f of the RC splitting parameters have been corrected for the effects of systematic error, as demonstrated in (a) and (b), by subtracting out the trend of the solid red line. These corrected results, plotted over the full 360° back azimuth range, are compared to predicted splitting parameters for entrained mantle flow for various anisotropic media described in the text (indicated by different colored dotted lines). In all cases the modeled anisotropic layer is 100-km thick, dipping at 30° with a down dip direction of 100° from north, based on the subduction geometry beneath the iMUSH array (Figure 9; Hayes et al., 2018). The shear direction is assumed to be parallel to the absolute plate motion of the Juan de Fuca plate as it subducts (dotted gray curves in Figure 8) which is $\sim 75^\circ$ beneath Mount St Helens. The dashed black line indicates the mean corrected Φ and ∂t values. RC = rotation correlation; SC = transverse component minimum energy method of Silver and Chan (1991); iMUSH = Imaging Magma under St. Helens.

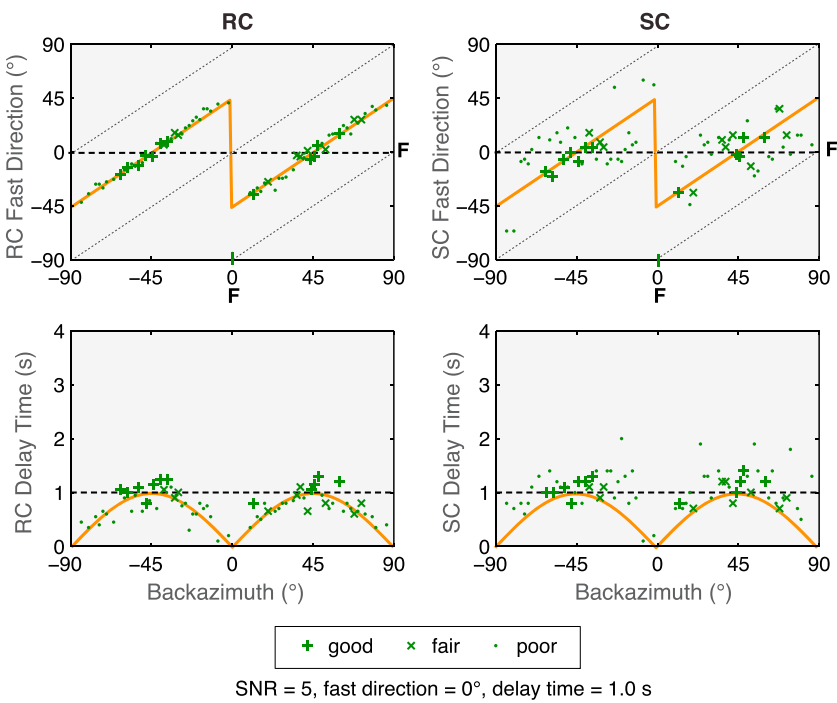


Figure 7. Results of a synthetic test by Wüstefeld and Bokelmann (2007) demonstrating the expected systematic back azimuthal variation of apparent splitting parameters from both the RC (left column) and SC (right column) measurement methods. Non-null measurements (green symbols) are retrieved for synthetic seismograms with a signal-to-noise ratio of 5, for a single anisotropic layer with a fast direction of 0° and delay time of 1.0 s (dashed black lines). The RC method produces a clear linear 45° trend in Φ and 90° periodicity in splitting parameters (orange line, plotted according to equations derived in section 4). The SC method follows a similar pattern, but the results are more scattered. Results are modified from Figures A7 and A8 of the supporting information of Wüstefeld and Bokelmann (2007). RC = rotation correlation; SC = transverse component minimum energy method of Silver and Chan (1991).

predictable as a function of back azimuth (orange line, Figure 7). The important characteristics are as follows: (1) the true Φ and δt values are found at back azimuths 45° away from the fast/slow axis orientations, (2) at all other back azimuths the apparent Φ follows a 45° slope except for a discontinuity at the fast axis orientation where a zero delay time also occurs, (3) Φ spans a range of $\pm 45^\circ$ from the true value. We can use these inherent characteristics to mathematically express the expected or apparent fast direction (Φ_{app}) and delay time (δt_{app}) as a function of the back azimuth (ψ) and the true values (Φ_{true} and δt_{true})

$$\Phi_{app} = \Phi_{true} - \frac{90}{\pi} \tan^{-1} \left(\cot \left(\frac{\pi}{90} (\psi - \Phi_{true}) \right) \right) \quad (1)$$

$$\delta t_{app} = \delta t_{true} * \left| \sin \left(\frac{\pi}{90} (\psi - \Phi_{true}) \right) \right| \quad (2)$$

where all angles are in degrees. The equation for the apparent fast direction is based on the general equation for a sawtooth wave with a period of 90° and an amplitude of 45° . The apparent delay time equation is based on the absolute value of a sine wave. It should be noted that we have empirically derived these equations based on the synthetic tests of Wüstefeld and Bokelmann (2007) for waveforms with a SNR of 5 and delay times on the order of 1.0 s (Figure 7). The form of the equations is expected to depend on both the noise level and the magnitude of delay times; higher SNR and larger delay times are expected to generate the true splitting parameters (i.e., a constant value) over an increasingly large range of back azimuths.

Comparing our empirically derived equations to our results produces an excellent match (red line on Figures 6a–6d). The best fit Φ_{true} and δt_{true} parameters of 73° and 1.1 s have been determined through a grid search and forward modeling. We compared our results against models with fast directions varying from

0:179° in 1° increments and delay times of 0:4 s in 0.1-s increments. The difference in the modeled and observed fast direction, and the delay time, is calculated for each data point and summed over all measurements to find the total misfit in Φ and in ∂t for each pair of model parameters (Figure S7). It is found that the minimum misfit in Φ occurs for model Φ_{true} values ranging from 60–78° (Figure S7a). This is constrained by the possible location of the sharp change or discontinuity in Φ in Figure 6a. The minimum misfit in ∂t further suggests that within this range the best-fit Φ_{true} value is 73° (Figure S7b), which is very similar to the previously determined mean value of the data set (74°). The minimum misfit in ∂t also suggests a best-fit model ∂t_{true} value of 1.1 s (Figure S7c), again very similar to the mean value of the observational data set (1.0 s).

Using these best-fit Φ_{true} and ∂t_{true} model parameters and our equations for the apparent splitting parameters Φ_{app} and ∂t_{app} we can then correct our measurements for the systematic error in the RC method (Figures 6e and 6f). Any back azimuthal variations remaining should therefore reflect anisotropic structure rather than measurement error. The corrected results now follow a flat line (i.e., invariant to back azimuth) consistent with a single layer of anisotropy.

To the best of our knowledge, this is the first time a 90° periodicity in splitting parameters with a 45° slope with respect to back azimuth has been robustly observed and described in a real data set. This is likely due to the limited back azimuthal coverage per station of most SKS studies limited by the availability of global seismicity. We have been partially able to overcome this by combining results across the dense iMUSH array. Each station only records an average of one split and six nulls across the 2-year time window, but the particular events that record results can vary slightly between stations (likely dependent on local noise conditions at each site). When the results from all the stations are combined, this encompasses a much wider range of back azimuths than is available at any one particular station. With such a well-sampled back azimuthal range our results confirm that even a single layer of anisotropy can produce strong back azimuthal variations with 90° periodicity that could otherwise be misinterpreted as a sign of more complex anisotropy, for example, multiple layers. It should however be easy to distinguish between systematic errors in the RC method and multiple anisotropic layers as the former will follow a strict 45° trend ($\Phi = \text{back azimuth} \pm 45^\circ$).

5. Discussion

Given the overall properties of our shear wave splitting results and outcome of our forward modeling (Figure 6), we infer the presence of a substantial layer of anisotropy beneath MSH, enough to generate ~1 s of splitting time, with an ENE-WSW fast direction of ~73°. Given that most of the corrected results now conform to a mean value (i.e., follow the dashed black line in Figures 6e–6f), it is unlikely that steep dips or additional significant layers of anisotropy exist beneath MSH, unless the layers have a similar fast direction. However, we cannot rule out the presence of other thin or weakly anisotropic layers, as might be expected in subduction zones.

As an example, a thin layer of anisotropic serpentinite has been inferred in the cold hydrated forearc mantle wedge of Cascadia by several seismic studies (Hansen et al., 2016; Krueger & Wirth, 2017; Nikulin et al., 2009; Park et al., 2004; Wagner et al., 2013). Most significantly, using sources and receivers from the active source component of the iMUSH array and studying Moho reflectivity, Hansen et al. (2016) inferred that MSH directly straddles the eastern inboard limit of the serpentized mantle wedge. The top of the Juan de Fuca slab, however, is only 68-km deep beneath Mount St. Helens (Mann et al., 2019), meaning that any serpentized layer can only be a few tens of kilometers thick. This is unlikely to be detected by SKS splitting, which has a minimal resolution of 0.5 s (~50 km for 4% anisotropy) for a typical characteristic frequency of 0.1 Hz (Eakin et al., 2018). This explains why we do not see any variability in shear wave splitting across the iMUSH array despite the possible presence of a serpentized mantle wedge toward the west (see Figure S6).

Other localities where a thin anisotropic layer is likely to exist, but we cannot constrain with SKS splitting, include the overriding plate (e.g., Balfour et al., 2012; Cassidy & Bostock, 1996; Matharu et al., 2014), and the subducting Juan de Fuca slab (Audet, 2013; Piana Agostinetti & Miller, 2014). The Juan de Fuca plate subducting at the trench is very young, less than 10 Myr old (Müller et al., 2008), and is therefore expected to be thin, less than 50-km thick according to lithospheric cooling models (Goes et al., 2013). Additionally, it

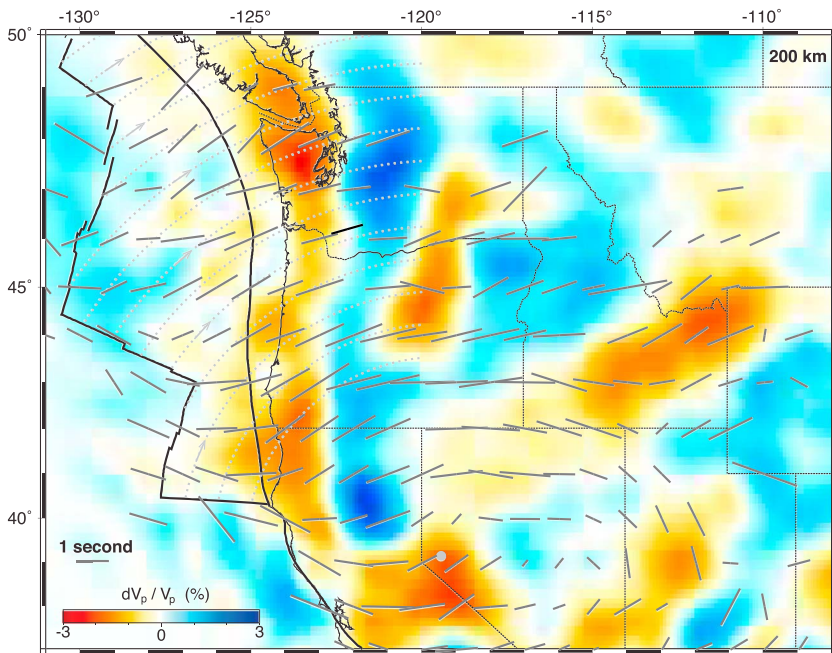


Figure 8. Regional splitting patterns across Cascadia and the western United States overlain on upper mantle velocity anomalies at 200-km depth. The mean splitting parameters retrieved from this study ($\Phi = 74^\circ$ and $\delta t = 1$ s) are shown by the black bar. Previous splitting results averaged over $1^\circ \times 1^\circ$ latitude and longitude bins are plotted in gray. These demonstrate a coherent splitting pattern throughout Cascadia that closely follow motion of the Juan de Fuca plate and its subduction. Averaged splitting is based on all prior results cataloged in the IRIS Shear-Wave Splitting Database (IRIS DMC, 2012) originating from a wide compilation of studies (Table S2). The velocity anomaly shown is a horizontal cross section at 200 km from the CASC16 P wave model (Hawley et al., 2016) highlighting the position of the Juan de Fuca slab at this depth (north-south high velocity feature in blue). Curved dotted gray lines represent the rotational nature of the absolute plate motion of the Juan de Fuca plate about its Euler pole (gray dot) as it subducts beneath North America (Gripp & Gordon, 2002). This figure is an updated version of Figure 2 in Eakin et al. (2010).

appears to be a relatively dry slab (Canales et al., 2017), particularly lacking in serpentinization of the lithospheric mantle from limited offshore bending faults, as is typically associated with strong intraslab anisotropy (e.g., Faccenda et al., 2008).

This leaves the subslab mantle as the most likely location for where our layer of ENE-WSW aligned anisotropy resides. Such a trench-normal anisotropic fast direction is very similar to the absolute plate motion of the subducting Juan de Fuca plate beneath MSH (~75° from north, Figure 8). This would be equivalent to the expected shear direction in the case of entrained subslab mantle flow. However, beneath our study area the Juan de Fuca slab is dipping at 30° toward the east (downdip direction of 100°) based on the most recent slab contours (Hayes et al., 2018). Any entrained mantle layer would be expected to possess a similar dipping geometry.

In Figures 6e and 6f we compare SKS splitting predictions against our corrected results for a range of possible anisotropic fabrics (dotted colored lines) under the geometrical assumptions of subslab entrainment and a layer thickness of 100 km. We compare predictions from six different elastic tensors. These include four different olivine LPO fabrics (A-, B-, C-, and E-types) derived from laboratory experiments exploring different physical and chemical conditions present in the upper mantle (Karato, 2008). We also compare predictions from natural samples of San Carlos olivine, which display single-crystal hexagonal symmetry characterized by a fast direction along the crystal a axis [100] (Abramson et al., 1997). Given that the anisotropic strength of a single crystal is considerably higher than that expected in the upper mantle where crystal alignment is imperfect, we dilute the anisotropy by a factor of 2.6 to achieve 4% anisotropy, consistent with natural peridotites (e.g., Christensen, 1984). Lastly, we include predictions from the entrained orthorhombic anisotropy model of Song and Kawakatsu (2012), which assumes that the suboceanic asthenosphere has combined azimuthal and radial anisotropy. In all cases the elastic tensor undergoes a 3-D

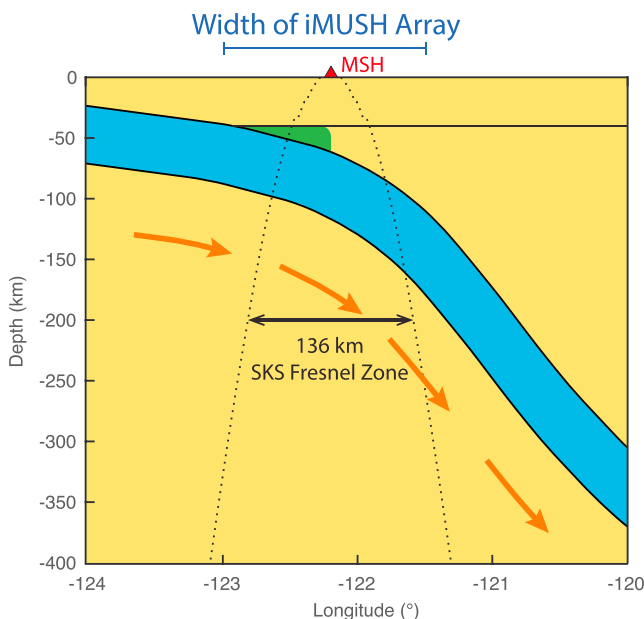


Figure 9. Schematic east-west cross section through the Cascadia subduction zone beneath Mount St. Helens illustrating inferred mantle flow entrained with the downgoing slab. The Fresnel zone of SKS waves at asthenospheric depths (~200 km) is calculated to be similar in lateral extent to the width of the iMUSH seismic array (Gudmundsson, 1996). Slab geometry is plotted based on the Slab2 model for Cascadia (Hayes et al., 2018). Extent of serpentinized mantle wedge as proposed by Hansen et al. (2016) is outlined in green. iMUSH = Imaging Magma under St. Helens.

away from the mid-ocean ridge (Bodmer et al., 2015; Martin-Short et al., 2015). Moreover, from the trench eastward, there is a progressive clockwise rotation of the fast splitting direction from NE-SW to E-W. This rotation in Φ matches the rotation of the absolute Juan de Fuca plate motion exceptionally well (dotted gray curved lines in Figure 8). The Euler pole of the Juan de Fuca plate in the hotspot mantle reference frame (Gripp & Gordon, 2002) is close by (39.2°N , 119.4°W ; gray dot in Figure 8), which generates a strong rotational motion. This factor is often overlooked by other studies that simply plot one arrow vector to capture the plate motion.

Previously, the change in fast direction from NE-SW in the forearc to E-W in the backarc, particularly beneath Oregon, has been cited as a crucial piece of evidence for large-scale toroidal mantle flow driven by slab rollback (Druken et al., 2011; Long, 2016; Long et al., 2009, 2012; Zandt & Humphreys, 2008). Considering the rotational motion of the Juan de Fuca slab and entrainment of the upper mantle, large-scale toroidal flow does not need to be invoked to explain the E-W splitting patterns. However, it may still be required to explain the unusual pattern of backarc volcanism in the High Lava Plains located at 43°N , 120°W (Long et al., 2012).

The exceptional consistency between the fast direction and the motion of the Juan de Fuca plate as it subducts suggests that there is coherent along-strike entrainment of the mantle asthenosphere by the downgoing slab (Figures 8 and 9). While entrained subslab mantle flow has occasionally been inferred from shear wave splitting in some other subduction settings (e.g., Eakin et al., 2015; Lynner & Long, 2014; Reiss et al., 2018; Soto et al., 2009), Cascadia is unique in the consistency and simplicity of its trench-normal splitting pattern seen throughout the entire subduction zone. This has several implications for the degree of coupling and style of interaction between the slab and the upper mantle in Cascadia versus other subduction zones globally.

First, it implies efficient and consistent coupling of the underlying asthenosphere with the subducting slab in order to produce such coherent splitting. This could be related to the prominent low-velocity asthenospheric material recently imaged beneath the Juan de Fuca plate at the Cascadia forearc (Bodmer et al., 2018;

rotation into the subduction geometry utilizing the calculations for a dipping anisotropic layer within the Matlab Seismic Anisotropy Toolbox, that is, MSAT (Walker & Wookey, 2012). Splitting parameters are predicted by solving the Christoffel equation for a given raypath (back azimuths ranging $0\text{--}360^{\circ}$, incidence angle: 10° , SKS period: 10 s) through the defined anisotropic medium.

We find that predictions from single crystal olivine (pink dotted line), and olivine LPO fabrics of A-type (purple) or E-Type (light blue) are consistent with our corrected results passing through the majority of measurements (Figures 6e and 6f). Predictions of an entrained layer of B-type (yellow) or C-type (red-orange) olivine LPO, or the orthorhombic anisotropy model of Song and Kawakatsu (2012; green) are found to be inconsistent with our results. We note that in any of these cases the delay times could be better matched by adjusting the layer thickness, but the current configuration illustrates the relative anisotropic strengths of each medium. Overall these models suggest that our results can be fully explained by an entrained upper mantle that is either dry (A-type) or moderately hydrated (E-type) and under ambient stress and temperature conditions (Karato et al., 2008). Olivine fabrics representing the most hydrated mantle states (C-type and B-type) can be ruled out.

We therefore infer that our ENE-WSW anisotropic fast direction most likely represents a layer of the asthenosphere (on the order of 100-km thick) entrained with the downgoing Juan de Fuca slab (Figures 7 and 8). Similar SKS splitting patterns are seen throughout the length and breadth of the Cascadia subduction zone (Figure 8). This includes offshore SKS splitting results that closely follow the Juan de Fuca plate motion suggesting the development of asthenospheric shear as the plate spreads

Hawley et al., 2016), and as seen west of the high-velocity slab in Figure 8. Widespread subslab entrainment would appear to contradict the authors' idea that this low-velocity region reflects buoyant low-viscosity material that may decouple the subducting plate from the underlying asthenosphere. Conversely, mantle viscosity may be dynamically lowered due to strong slab-induced mantle flow where the rheology is non-Newtonian and strain rate dependent, particularly close to slab edges (e.g., Jadamec, 2016). Nonetheless this north-south trending low-velocity anomaly is imaged along-strike underneath the slab down to 300 km suggesting at least some entrainment of the asthenospheric material to depth (Hawley et al., 2016).

Second, the fragmentation of the Juan de Fuca slab imaged by many studies is thought to be particularly important for the resulting mantle flow field (Pavlis et al., 2012); an example of the weak (or absent) slab anomaly beneath northern Oregon can be seen in Figure 8. This would provide an escape route for the entrained mantle flow either under the slab or through a slab gap as first suggested by Eakin et al. (2010) and Obrebski et al. (2010).

Lastly, a notable feature of the broader Cascadia splitting pattern is the striking change in fast direction at the Mendocino Triple Junction (MTJ) at the southern end of the Cascadia subduction zone (124°W, 40°N; Figure 8) suggestive of localized mantle flow around the slab edge (Eakin et al., 2010). Diversion of the asthenosphere around the southern edge of the Juan de Fuca slab is consistent not only with the pattern of SKS splitting but also with the curvature and continuation of the low-velocity anomaly from west to south of the slab (Figure 8; Hawley et al., 2016). Similar patterns have also been observed at the northern end of Cascadia (Mosher et al., 2014). This abrupt change in ENE-WSW fast directions where the slab ends lends further support to our argument that the detected anisotropy beneath MSH primarily reflects entrainment of the mantle with the subducting Juan de Fuca slab.

6. Conclusion

Analysis using the iMUSH array has provided an unprecedented density and azimuthal coverage of SKS splitting measurements beneath MSH in the Cascadia subduction zone. A 90° periodicity of splitting parameters with back azimuth has been revealed, which we demonstrated to be the result of systematic error inherent within the measurement method. The corrected results are consistent with a ~100-km-thick layer of the subslab mantle of either A-type or E-type olivine LPO fabric entrained with the downgoing Juan de Fuca plate. In Cascadia, pervasive entrainment of the subslab mantle is thought to be aided by the fragmented nature of the Juan de Fuca slab in the upper mantle and transition zone. This relationship can likely be further tested by combining mantle flow indicators with high-resolution images of tears, gaps, and holes in subducting slabs worldwide (e.g., Lynner et al., 2017). The outcome of this work will have implications for the degree of coupling between slab fragments and the surrounding mantle flow field and, in general, for subducting slabs as drivers of the global mantle convection system. This is likely to have important consequences for volcanism and dynamic topography in subduction zones and the associated patterns of surface topography and deformation (Eakin & Lithgow-Bertelloni, 2018).

References

- Abramson, E. H., Brown, J. M., Slutsky, L. J., & Zaug, J. (1997). The elastic constants of San Carlos olivine to 17 GPa. *Journal of Geophysical Research*, 102(B6), 12,253–12,263. <https://doi.org/10.1029/97JB00682>
- Atwater, B. F., Musumi-Rokkaku, S., Satake, K., Tsuji, Y., Ueda, K., & Yamaguchi, D. K. (2005). The orphan tsunami of 1700—Japanese clues to a parent earthquake in North America. U.S. Geological Survey Professional Paper 1707. Seattle. <https://doi.org/10.3133/pp1707>
- Audet, P. (2013). Seismic anisotropy of subducting oceanic uppermost mantle from fossil spreading. *Geophysical Research Letters*, 40, 173–177. <https://doi.org/10.1029/2012GL054328>
- Balfour, N. J., Cassidy, J. F., & Dosso, S. E. (2012). Crustal anisotropy in the forearc of the Northern Cascadia Subduction Zone, British Columbia. *Geophysical Journal International*, 188(1), 165–176. <https://doi.org/10.1111/j.1365-246X.2011.05231.x>
- Bodmer, M., Toomey, D. R., Hooft, E. E., Nabelek, J., & Braumiller, J. (2015). Seismic anisotropy beneath the Juan de Fuca plate system: Evidence for heterogeneous mantle flow. *Geology*, 43(12), G37181.1. <https://doi.org/10.1130/G37181.1>
- Bodmer, M., Toomey, D. R., Hooft, E. E. E., & Schmandt, B. (2018). Buoyant asthenosphere beneath Cascadia influences megathrust segmentation. *Geophysical Research Letters*, 45(14), 6954–6962. <https://doi.org/10.1029/2018GL078700>
- Bowman, J. R., & Ando, M. (1987). Shear-wave splitting in the upper-mantle wedge above the Tonga subduction zone. *Geophysical Journal International*, 88(1), 25–41. <https://doi.org/10.1111/j.1365-246X.1987.tb01367.x>
- Canales, J. P., Carbotte, S. M., Nedimović, M. R., & Carton, H. (2017). Dry Juan de Fuca slab revealed by quantification of water entering Cascadia subduction zone. *Nature Geoscience*, 10(11), 864–870. <https://doi.org/10.1038/ngeo3050>
- Cassidy, J. F., & Bostock, M. G. (1996). Shear-wave splitting above the subducting Juan de Fuca Plate. *Geophysical Research Letters*, 23(9), 941–944. <https://doi.org/10.1029/96GL00976>

Acknowledgments

We thank Rob Porritt and Laureen Waszek for providing early reviews of this manuscript, in addition to three anonymous reviewers and the editor for their constructive and helpful comments. Splitting measurements were made using SplitLab version 1.2 updated by Rob Porritt and available for download here (<https://robporritt.wordpress.com/software/>). Figures were made with the aid of Generic Mapping tools (Wessel et al., 2013). We thank William B. Hawley for sharing the tomographic depth-slice used in Figure 8. The broadband seismic component of the iMUSH project was supported by National Science Foundation grants EAR-1144568, EAR-1144351, EAR-1460291, and EAR-1444275. CME acknowledges support from the Australian Research Council (DE190100062). We thank the 2017 IRIS undergraduate summer intern program for providing support to A. W. to work with E. A. W. at the University of Washington. The facilities of IRIS Data Services, and specifically the IRIS Data Management Center, were used for access to waveforms, related metadata, and/or derived products used in this study. IRIS Data Services are funded through the Seismological Facilities for the Advancement of Geoscience and EarthScope (SAGE) Proposal of the National Science Foundation under Cooperative Agreement EAR-1261681. Seismic networks which provided the data for this study include the iMUSH broadband array (network code: XD; https://doi.org/10.7914/SN/XD_2014), the Cascades Volcano Observatory Station (CVO; network code: CC; <https://doi.org/10.7914/SN/CC>), and the Pacific Northwest Seismic Network at the University of Washington (network code: UW; <https://doi.org/10.7914/SN/UW>). A table of the shear wave splitting measurements made during this study can be found in the supporting information (Table S1).

- Christensen, N. (1984). The magnitude, symmetry and origin of upper mantle anisotropy based on fabric analyses of ultramafic tectonites. *Geophysical Journal International*, 76(1), 89–111. <https://doi.org/10.1111/j.1365-246X.1984.tb05025.x>
- Crampin, S. (1994). The fracture criticality of crustal rocks. *Geophysical Journal International*, 118(2), 428–438. <https://doi.org/10.1111/j.1365-246X.1994.tb03974.x>
- Creager, K. C., Ulberg, C. W., Vidale, J. E., Levander, A., Kiser, E., Abers, G. A., et al. (2017). Comparing three-dimensional geophysical models of Mount St. Helens. In *American Geophysical Union, Fall Meeting 2017, abstract #V11C-0368*. New Orleans.
- Currie, C. A., Cassidy, J. F., Hyndman, R. D., & Bostock, M. G. (2004). Shear wave anisotropy beneath the Cascadia subduction zone and western North American craton. *Geophysical Journal International*, 157(1), 341–353. <https://doi.org/10.1111/j.1365-246X.2004.02175.x>
- Druken, K. A., Long, M. D., & Kincaid, C. (2011). Patterns in seismic anisotropy driven by rollback subduction beneath the High Lava Plains. *Geophysical Research Letters*, 38, L13310. <https://doi.org/10.1029/2011GL047541>
- Eakin, C. M., & Lithgow-Bertelloni, C. (2018). An overview of dynamic topography: The influence of mantle circulation on surface topography and landscape. In C. Hoorn, A. Perrigo, & A. Antonelli (Eds.), *Mountains, Climate, and Biodiversity* (pp. 37–49). Hoboken, NJ: John Wiley and Sons.
- Eakin, C. M., & Long, M. D. (2013). Complex anisotropy beneath the Peruvian flat slab from frequency-dependent, multiple-phase shear wave splitting analysis. *Journal of Geophysical Research: Solid Earth*, 118, 4794–4813. <https://doi.org/10.1002/jgrb.50349>
- Eakin, C. M., Long, M. D., Wagner, L. S., Beck, S. L., & Tavera, H. (2015). Upper mantle anisotropy beneath Peru from SKS splitting: Constraints on flat slab dynamics and interaction with the Nazca Ridge. *Earth and Planetary Science Letters*, 412, 152–162. <https://doi.org/10.1016/j.epsl.2014.12.015>
- Eakin, C. M., Obrebski, M., Allen, R. M., Boyarko, D. C., Brudzinski, M. R., & Porritt, R. (2010). Seismic anisotropy beneath Cascadia and the Mendocino triple junction: Interaction of the subducting slab with mantle flow. *Earth and Planetary Science Letters*, 297, 627–632. <https://doi.org/10.1016/j.epsl.2010.07.015>
- Eakin, C. M., Rychert, C. A., & Harmon, N. (2018). The role of oceanic transform faults in seafloor spreading: A global perspective from seismic anisotropy. *Journal of Geophysical Research: Solid Earth*, 123, 1736–1751. <https://doi.org/10.1002/2017JB015176>
- Faccenda, M., Burlini, L., Gerya, T. V., & Mainprice, D. (2008). Fault-induced seismic anisotropy by hydration in subducting oceanic plates. *Nature*, 455(7216), 1097–1100. <https://doi.org/10.1038/nature07376>
- Frankel, A., Wirth, E. A., Marafi, N., Vidale, J., & Stephenson, W. (2018). Broadband synthetic seismograms for magnitude 9 earthquakes on the Cascadia megathrust based on 3D simulations and stochastic synthetics. Part 1: Methodology and overall results. *Bulletin of the Seismological Society of America*, 108, 2347–2369. <https://doi.org/10.1785/0120180034>
- Goes, S., Eakin, C. M., & Ritsema, J. (2013). Lithospheric cooling trends and deviations in oceanic PP-P and SS-S differential traveltimes. *Journal of Geophysical Research: Solid Earth*, 118, 996–1007. <https://doi.org/10.1002/jgrb.50092>
- Goldfinger, C., Nelson, C. H., Morey, A. E., Johnson, J. E., Patton, J. R., Karabonov, E., et al. (2012). Turbidite event history — Methods and implications for Holocene paleoseismicity of the Cascadia subduction zone. *U.S. Geological Survey Professional Paper 1661-F* (p. 170). Reston, VA: U.S. Geological Survey. Retrieved from <https://pubs.usgs.gov/pp/1661f/>
- Gripp, A. E., & Gordon, R. G. (2002). Young tracks of hotspots and current plate velocities. *Geophysical Journal International*, 150(2), 321–361. <https://doi.org/10.1046/j.1365-246X.2002.01627.x>
- Guðmundsson, O. (1996). On the effect of diffraction on traveltime measurements. *Geophysical Journal International*, 124(1), 304–314. <https://doi.org/10.1111/j.1365-246X.1996.tb06372.x>
- Hansen, S. M., Schmandt, B., Levander, A., Kiser, E., Vidale, J. E., Abers, G. A., & Creager, K. C. (2016). Seismic evidence for a cold serpentized mantle wedge beneath Mount St Helens. *Nature Communications*, 7, 13242. <https://doi.org/10.1038/ncomms13242>
- Hawley, W. B., Allen, R. M., & Richards, M. A. (2016). Tomography reveals buoyant asthenosphere accumulating beneath the Juan de Fuca plate. *Science*, 353, 1406–1408. <https://doi.org/10.1126/science.aad8104>
- Hayes, G. P., Moore, G. L., Portner, D. E., Hearne, M., Flamme, H., Furtney, M., & Smoczyk, G. M. (2018). Slab2, a comprehensive subduction zone geometry model. *Science*, 362, 58–61. <https://doi.org/10.1126/science.aat4723>
- IRIS DMC (2012). Data Services Products: SWS-DBs Shear-wave splitting databases. <https://doi.org/10.17611/DP/SWS.1>
- Jadamec, M. A. (2016). Insights on slab-driven mantle flow from advances in three-dimensional modelling. *Journal of Geodynamics*, 100, 51–70. <https://doi.org/10.1016/J.JOG.2016.07.004>
- Karato, S. (2008). *Deformation of earth materials. An introduction to the rheology of solid earth*. Cambridge, UK: Cambridge University Press. <https://doi.org/10.1017/CBO9780511804892>
- Karato, S., Jung, H., Katayama, I., & Skemer, P. (2008). Geodynamic significance of seismic anisotropy of the upper mantle: New insights from laboratory studies. *Annual Review of Earth and Planetary Sciences*, 36, 59–95. <https://doi.org/10.1146/annurev.earth.36.031207.124120>
- Kendall, J. M., & Silver, P. G. (1996). Constraints from seismic anisotropy on the nature of the lowermost mantle. *Nature*, 381(6581), 409–412. <https://doi.org/10.1038/381409a0>
- Krueger, H. E., & Wirth, E. A. (2017). Investigating segmentation in Cascadia: Anisotropic crustal structure and mantle wedge serpentization from receiver functions. *Geochemistry, Geophysics, Geosystems*, 18, 3592–3607. <https://doi.org/10.1002/2017GC007064>
- Liu, K. H., & Gao, S. S. (2013). Making reliable shear-wave splitting measurements. *Bulletin of the Seismological Society of America*, 103, 2680–2693. <https://doi.org/10.1785/0120120355>
- Long, M. D. (2016). The Cascadia paradox: Mantle flow and slab fragmentation in the Cascadia subduction system. *Journal of Geodynamics*, 102, 151–170. <https://doi.org/10.1016/J.JOG.2016.09.006>
- Long, M. D., & Becker, T. W. (2010). Mantle dynamics and seismic anisotropy. *Earth and Planetary Science Letters*, 297, 341–354. <https://doi.org/10.1016/j.epsl.2010.06.036>
- Long, M. D., Gao, H., Klaus, A., Wagner, L. S., Fouch, M. J., James, D. E., & Humphreys, E. (2009). Shear wave splitting and the pattern of mantle flow beneath eastern Oregon. *Earth and Planetary Science Letters*, 288(3–4), 359–369. <https://doi.org/10.1016/J.EPSL.2009.09.039>
- Long, M. D., & Silver, P. G. (2008). The subduction zone flow field from seismic anisotropy: A global view. *Science*, 319, 315–318. <https://doi.org/10.1126/science.1150809>
- Long, M. D., & Silver, P. G. (2009). Mantle flow in subduction systems: The subslab flow field and implications for mantle dynamics. *Journal of Geophysical Research*, 114, B10312. <https://doi.org/10.1029/2008JB006200>
- Long, M. D., Till, C. B., Druken, K. A., Carlson, R. W., Wagner, L. S., Fouch, M. J., et al. (2012). Mantle dynamics beneath the Pacific Northwest and the generation of voluminous back-arc volcanism. *Geochemistry, Geophysics, Geosystems*, 13, Q0AN01. <https://doi.org/10.1029/2012GC004189>

- Lynner, C., Anderson, M. L., Portner, D. E., Beck, S. L., & Gilbert, H. (2017). Mantle flow through a tear in the Nazca slab inferred from shear wave splitting. *Geophysical Research Letters*, 44, 6735–6742. <https://doi.org/10.1002/2017GL074312>
- Lynner, C., & Long, M. D. (2014). Sub-slab anisotropy beneath the Sumatra and circum-Pacific subduction zones from source-side shear wave splitting observations. *Geochemistry, Geophysics, Geosystems*, 15, 2262–2281. <https://doi.org/10.1029/2014GC005239>
- Mainprice, D., & Ildefonse, B. (2009). Seismic anisotropy of subduction zone minerals—contribution of hydrous phases. In S. Lallemand, & F. Fumicello (Eds.), *Subduction zone geodynamics*, (pp. 63–84). Berlin Heidelberg: Springer. https://doi.org/10.1007/978-3-540-87974-9_4
- Mann, M. E., Abers, G. A., Crosbie, K., Creager, K., Ulberg, C., Moran, S., & Rondenay, S. (2019). Imaging subduction beneath Mount St. Helens: Implications for slab dehydration and magma transport. *Geophysical Research Letters*, 46, 3163–3171. <https://doi.org/10.1029/2018GL081471>
- Martin-Short, R., Allen, R. M., Bastow, I. D., Totten, E., & Richards, M. A. (2015). Mantle flow geometry from ridge to trench beneath the Gorda–Juan de Fuca plate system. *Nature Geoscience*, 8, 965–968. <https://doi.org/10.1038/ngeo2569>
- Matharu, G., Bostock, M. G., Christensen, N. I., & Tromp, J. (2014). Crustal anisotropy in a subduction zone forearc: Northern Cascadia. *Journal of Geophysical Research: Solid Earth*, 119, 7058–7078. <https://doi.org/10.1002/2014JB011321>
- McCormack, K., Wirth, E. A., & Long, M. D. (2013). B-type olivine fabric and mantle wedge serpentinization beneath the Ryukyu arc. *Geophysical Research Letters*, 40, 1697–1702. <https://doi.org/10.1002/grl.50369>
- Menke, W., & Levin, V. (2003). The cross-convolution method for interpreting SKS splitting observations, with application to one and two-layer anisotropic Earth models. *Geophysical Journal International*, 154(2), 379–392. <https://doi.org/10.1046/j.1365-246X.2003.01937.x>
- Monteiller, V., & Chevrot, S. (2010). How to make robust splitting measurements for single-station analysis and three-dimensional imaging of seismic anisotropy. *Geophysical Journal International*, 182, 311–328. <https://doi.org/10.1111/j.1365-246X.2010.04608.x>
- Mosher, S. G., Audet, P., & L'Heureux, I. (2014). Seismic evidence for rotating mantle flow around subducting slab edge associated with oceanic microplate capture. *Geophysical Research Letters*, 41, 4548–4553. <https://doi.org/10.1002/2014GL060630>
- Müller, R., Sdrolias, M., Gaina, C., & Roest, W. (2008). Age, spreading rates, and spreading asymmetry of the world's ocean crust. *Geochemistry, Geophysics, Geosystems*, 9, Q04006. <https://doi.org/10.1029/2007GC001743>
- Nicolas, A., & Christensen, N. I. (1987). Formation of anisotropy in upper mantle peridotites: A review. In *Composition, structure and dynamics of the lithosphere–asthenosphere system* (pp. 111–123). Washington, DC: American Geophysical Union. <https://doi.org/10.1029/GD016p0111>
- Nikulin, A., Levin, V., & Park, J. (2009). Receiver function study of the Cascadia megathrust: Evidence for localized serpentinization. *Geochemistry, Geophysics, Geosystems*, 10, Q07004. <https://doi.org/10.1029/2009GC002376>
- Obrebski, M., Allen, R. M., Xue, M., & Hung, S.-H. (2010). Slab-plume interaction beneath the Pacific Northwest. *Geophysical Research Letters*, 37, L14305. <https://doi.org/10.1029/2010GL043489>
- Park, J., Yuan, H., & Levin, V. (2004). Subduction zone anisotropy beneath Corvallis, Oregon: A serpentinite skid mark of trench-parallel terrane migration? *Journal of Geophysical Research*, 109, B10306. <https://doi.org/10.1029/2003JB002718>
- Pavlis, G. L., Sigloch, K., Burdick, S., Fouch, M. J., & Vernon, F. L. (2012). Unraveling the geometry of the Farallon plate: Synthesis of three-dimensional imaging results from USArray. *Tectonophysics*, 532–535, 82–102. <https://doi.org/10.1016/J.TECTO.2012.02.008>
- Piana Agostinetti, N., & Miller, M. S. (2014). The fate of the downgoing oceanic plate: Insight from the Northern Cascadia subduction zone. *Earth and Planetary Science Letters*, 408, 237–251. <https://doi.org/10.1016/J.EPSL.2014.10.016>
- Reiss, M. C., Rümpker, G., & Wölbern, I. (2018). Large-scale trench-normal mantle flow beneath central South America. *Earth and Planetary Science Letters*, 482, 115–125. <https://doi.org/10.1016/J.EPSL.2017.11.002>
- Rieger, D. M., & Park, J. (2010). USArray observations of quasi-Love surface wave scattering: Orienting anisotropy in the Cascadia plate boundary. *Journal of Geophysical Research*, 115, B05306. <https://doi.org/10.1029/2009JB006754>
- Restivo, A., & Helffrich, G. (1999). Teleseismic shear wave splitting measurements in noisy environments. *Geophysical Journal International*, 137(3), 821–830. <https://doi.org/10.1046/j.1365-246x.1999.00845.x>
- Schellart, W. P., Stegman, D. R., & Freeman, J. (2008). Global trench migration velocities and slab migration induced upper mantle volume fluxes: Constraints to find an Earth reference frame based on minimizing viscous dissipation. *Earth-Science Reviews*, 88, 118–144. <https://doi.org/10.1016/j.earscirev.2008.01.005>
- Severinghaus, J., & Atwater, T. (1990). Cenozoic geometry and thermal state of the subducting slabs beneath western North America. In *Basin and range extensional tectonics near the latitude of Las Vegas, Nevada*, (Vol. 176, pp. 1–22). California: Geological Society of America Memoir. <https://doi.org/10.1130/MEM176-p1>
- Siebert, L., & Simkin, T. (2002). Volcanoes of the world: An illustrated catalog of Holocene volcanoes and their eruptions. *Global Volcanism Program Digital Information Series, GVP-3*. Washington, DC: Smithsonian Institution. http://volcano.si.edu/search_vcano.cfm
- Silver, P. G., & Chan, W. W. (1991). Shear wave splitting and sub continental mantle deformation. *Journal of Geophysical Research*, 96(B10), 16,429–16,454. <https://doi.org/10.1029/91JB00899>
- Song, T.-R. A., & Kawakatsu, H. (2012). Subduction of oceanic asthenosphere: Evidence from sub-slab seismic anisotropy. *Geophysical Research Letters*, 39, L17301. <https://doi.org/10.1029/2012GL052639>
- Soto, G. L., Ni, J. F., Grand, S. P., Sandvol, E., Valenzuela, R. W., Speziale, M. G., et al. (2009). Mantle flow in the Rivera-Cocos subduction zone. *Geophysical Journal International*, 179, 1004–1012. <https://doi.org/10.1111/j.1365-246X.2009.04352.x>
- Ulberg, C. W., Creager, K. C., Moran, S. C., Abers, G. A., Crosbie, K., Crosson, R. S., et al. (2017). Imaging seismic zones and magma beneath Mount St. Helens with the iMUSH broadband array. In *American Geophysical Union, Fall Meeting 2017, abstract #V1C-0367*. New Orleans.
- Vecsey, L., Plomerová, J., & Babuška, V. (2008). Shear-wave splitting measurements — Problems and solutions. *Tectonophysics*, 462, 178–196. <https://doi.org/10.1016/J.TECTO.2008.01.021>
- Vinnik, L. P., Makeyeva, L. I., Milev, A., & Usenko, A. Y. (1992). Global patterns of azimuthal anisotropy and deformations in the continental mantle. *Geophysical Journal International*, 111(3), 433–447. <https://doi.org/10.1111/j.1365-246X.1992.tb02102.x>
- Wagner, L. S., Fouch, M. J., James, D. E., & Long, M. D. (2013). The role of hydrous phases in the formation of trench parallel anisotropy: Evidence from Rayleigh waves in Cascadia. *Geophysical Research Letters*, 40, 2642–2646. <https://doi.org/10.1002/grl.50525>
- Walker, A. M., & Wooley, J. (2012). MSAT—A new toolkit for the analysis of elastic and seismic anisotropy. *Computers & Geosciences*, 49, 81–90. <https://doi.org/10.1016/j.cageo.2012.05.031>
- Wessel, P., Smith, W. H. F., Scharroo, R., Luis, J., & Wobbe, F. (2013). Generic mapping tools: Improved version released. *Eos, Transactions American Geophysical Union*, 94, 409–410. <https://doi.org/10.1002/2013EO450001>

- Wirth, E. A., Frankel, A. D., Marafi, N., Vidale, J. E., & Stephenson, W. J. (2018). Broadband synthetic seismograms for magnitude 9 earthquakes on the Cascadia megathrust based on 3D simulations and stochastic synthetics, Part 2: Rupture parameters and variability. *Bulletin of the Seismological Society of America*, 108, 2370–2388. <https://doi.org/10.1785/0120180029>
- Wirth, E. A., & Long, M. D. (2010). Frequency-dependent shear wave splitting beneath the Japan and Izu-Bonin subduction zones. *Physics of the Earth and Planetary Interiors*, 181, 141–154. <https://doi.org/10.1016/j.pepi.2010.05.006>
- Wüstefeld, A., & Bokelmann, G. (2007). Null detection in shear-wave splitting measurements. *Bulletin of the Seismological Society of America*, 97, 1204–1211. <https://doi.org/10.1785/0120060190>
- Wüstefeld, A., Bokelmann, G., Zaroli, C., & Barruol, G. (2008). SplitLab: A shear-wave splitting environment in Matlab. *Computers & Geosciences*, 34, 515–528. <https://doi.org/10.1016/j.cageo.2007.08.002>
- Zandt, G., & Humphreys, E. (2008). Toroidal mantle flow through the western U.S. slab window. *Geology*, 36, 295. <https://doi.org/10.1130/G24611A.1>
- Zhang, S., & Karato, S. (1995). Lattice preferred orientation of olivine aggregates deformed in simple shear. *Nature*, 375(6534), 774–777. <https://doi.org/10.1038/375774a0>

References from the Supporting Information

- Barak, S., & Klemperer, S. L. (2016). Rapid variation in upper-mantle rheology across the San Andreas fault system and Salton Trough, southernmost California, USA. *Geology*, 44(7), 575–578. <https://doi.org/10.1130/G37847.1>
- Barruol, G., & Hoffmann, R. (1999). Upper mantle anisotropy beneath the Geoscope stations. *Journal of Geophysical Research*, 104(B5), 10,757–10,773. <https://doi.org/10.1029/1999JB900033>
- Barruol, G., Silver, P. G., & Vauchez, A. (1997). Seismic anisotropy in the eastern United States: Deep structure of a complex continental plate. *Journal of Geophysical Research*, 102(B4), 8329–8348. <https://doi.org/10.1029/96JB03800>
- Bonnin, M., Barruol, G., & Bokelmann, G. H. R. (2010). Upper mantle deformation beneath the North American–Pacific plate boundary in California from SKS splitting. *Journal of Geophysical Research*, 115, B04306. <https://doi.org/10.1029/2009JB006438>
- Bostock, M. G., & Cassidy, J. F. (1995). Variations in SKS splitting across western Canada. *Geophysical Research Letters*, 22(1), 5–8. <https://doi.org/10.1029/94GL02789>
- Davis, P. M. (2003). Azimuthal variation in seismic anisotropy of the southern California uppermost mantle. *Journal of Geophysical Research*, 108(B1), 2052. <https://doi.org/10.1029/2001JB000637>
- Gök, R., Ni, J. F., West, M., Sandvol, E., Wilson, D., Aster, R., et al. (2003). Shear wave splitting and mantle flow beneath LA RISTRA. *Geophysical Research Letters*, 30(12), 1614. <https://doi.org/10.1029/2002GL016616>
- Hartog, R., & Schwartz, S. Y. (2000). Subduction-induced strain in the upper mantle east of the Mendocino triple junction, California. *Journal of Geophysical Research*, 105(B4), 7909–7930. <https://doi.org/10.1029/1999JB900422>
- Jiang, C., Schmandt, B., & Clayton, R. W. (2018). An Anisotropic Contrast in the Lithosphere Across the Central San Andreas Fault. *Geophysical Research Letters*, 45, 3967–3975. <https://doi.org/10.1029/2018GL077476>
- Liu, H., Davis, P. M., & Gao, S. (1995). SKS splitting beneath southern California. *Geophysical Research Letters*, 22(7), 767–770. <https://doi.org/10.1029/95GL00487>
- Marone, F., & Romanowicz, B. (2007). The depth distribution of azimuthal anisotropy in the continental upper mantle. *Nature*, 447(7141), 198–201. <https://doi.org/10.1038/nature05742>
- Monteiller, V., & Chevrot, S. (2011). High-resolution imaging of the deep anisotropic structure of the San Andreas Fault system beneath southern California. *Geophysical Journal International*, 186(2), 418–446. <https://doi.org/10.1111/j.1365-246X.2011.05082.x>
- Özalaybey, S., & Savage, M. K. (1995). Shear-wave splitting beneath western United States in relation to plate tectonics. *Journal of Geophysical Research*, 100(B9), 18,135–18,149. <https://doi.org/10.1029/95JB00715>
- Ramsay, J., Kohler, M. D., Davis, P. M., Wang, X., Holt, W., & Weeraratne, D. S. (2016). Anisotropy from SKS splitting across the Pacific–North America plate boundary offshore southern California. *Geophysical Journal International*, 207(1), 244–258. <https://doi.org/10.1093/gji/ggw271>
- Ruppert, S. (1992). *Shear wave splitting and subcontinental mantle deformation*. (Doctoral dissertation). Stanford, CA: Stanford University. Retrieved from IRIS Shear-Wave Splitting Database <https://doi.org/10.17611/DP/SWS.1>
- Sandvol, E., & Ni, J. (1994). Mapping seismic azimuthal anisotropy in the United States from LRSR short period data. *Eos, Transactions, American Geophysical Union*, 75, 481. <https://doi.org/10.1029/2019GC008433>
- Savage, M. K., & Sheehan, A. F. (2000). Seismic anisotropy and mantle flow from the Great Basin to the Great Plains, western United States. *Journal of Geophysical Research*, 105(B6), 13,715–13,734. <https://doi.org/10.1029/2000JB900021>
- Savage, M. K., & Silver, P. G. (1993). Mantle deformation and tectonics: constraints from seismic anisotropy in western United States. *Geophysical Journal International*, 111, 433–447.
- Savage, M. K., Sheehan, A. F., & Lerner-Lam, A. (1996). Shear wave splitting across the Rocky Mountain Front. *Geophysical Research Letters*, 23(17), 2267–2270. <https://doi.org/10.1029/96GL02146>
- Schutt, D., Humphreys, E. D., & Dueker, K. (1998). Anisotropy of the Yellowstone Hot Spot Wake, Eastern Snake River Plain, Idaho. In *Geodynamics of Lithosphere & Earth's Mantle*, (pp. 443–462). Basel: Birkhäuser Basel. https://doi.org/10.1007/978-3-0348-8777-9_11
- Silver, P. G., & Savage, M. K. (1994). The Interpretation of Shear-Wave Splitting Parameters In the Presence of Two Anisotropic Layers. *Geophysical Journal International*, 119(3), 949–963. <https://doi.org/10.1111/j.1365-246X.1994.tb04027.x>
- Waite, G. P., Schutt, D. L., & Smith, R. B. (2005). Models of lithosphere and asthenosphere anisotropic structure of the Yellowstone hot spot from shear wave splitting. *Journal of Geophysical Research*, 110, B11304. <https://doi.org/10.1029/2004JB003501>
- Walker, K. T., Bokelmann, G. H. R., & Klemperer, S. L. (2004). Shear-wave splitting beneath the Snake River Plain suggests a mantle upwelling beneath eastern Nevada, USA. *Earth and Planetary Science Letters*, 222(2), 529–542. <https://doi.org/10.1016/J.EPSL.2004.03.024>
- West, J. D., Fouch, M. J., Roth, J. B., & Elkins-Tanton, L. T. (2009). Vertical mantle flow associated with a lithospheric drip beneath the Great Basin. *Nature Geoscience*, 2(6), 439–444. <https://doi.org/10.1038/ngeo526>